Electronic properties of corrugated graphene.

F.Guinea

A. Castro-Neto (Boston U.), N. M. R. Peres (U. Minho, Portugal), E. V. Castro, J. dos Santos (Porto), J. Nilsson (Boston U.), A. Morpurgo (Delft), **M. I. Katsnelson** (Nijmegen), D. Huertas-Hernando (Trondheim, Norway), D. P. Arovas, **M. M. Fogler** (U. C. San Diego), **F. von Oppen** (Berlin), **A. Akhmerov** (Leyden), J. González, F. G., **G. León**, M. P. López-Sancho, T. Stauber, J. A. Vergés, **M. A. H. Vozmediano**, B Wunsch (CSIC, Madrid), **A. K. Geim**, K. S. Novoselov (U. Manchester), A. Lanzara (U. C. Berkeley), M. Hentschel (Dresden), **E. Prada, P. San-José** (Karlsruhe, Lancaster), J. L. Mañes (U. País Vasco, Spain), F. Sols (U. Complutense, Madrid), E. Louis (U. Alicante, Spain), A. L. Vázquez de Parga, R. Miranda (U. Autónoma, Madrid), **B. Horovitz** (Beersheva), **P. Le Doussal** (ENS, Paris), A. K. Savchenko (Exeter).

KITPGraphene week.
Apr. 13-17, 2009

- Midgap states in graphene quantum dots (with A. Akhmerov)
- Effective electric fields (with F. von Oppen, E. Mariani)
- Effective and real magnetic fields in suspended graphene samples (with M. Fogler, M. I. Katsnelson, G. León, E. Prada, P. San José, A. K. Geim)

Localized states at edges

M. Fujita, K. Wakabayashi, K. Nakada, and K. Kusakabe,
Journ. Phys. Soc. Jap. **65**, 1920 (1996)

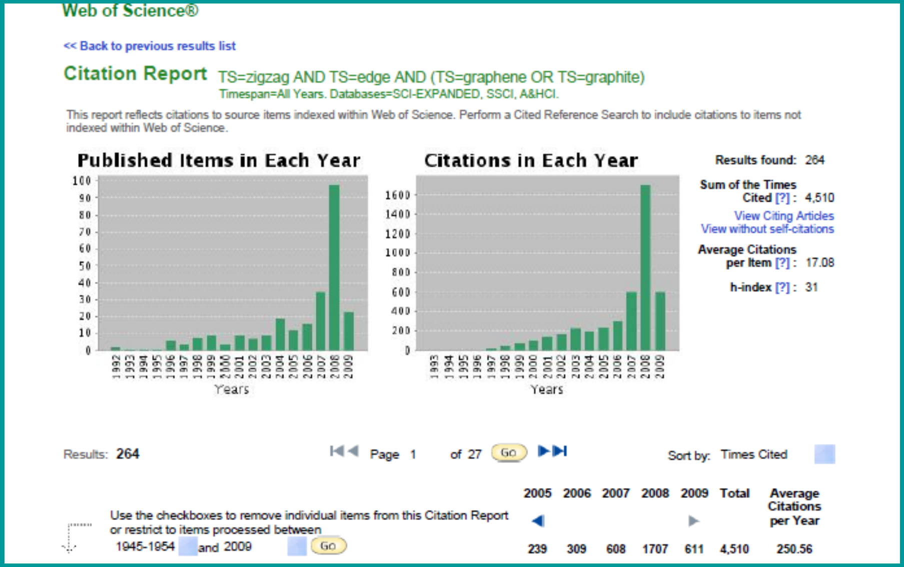

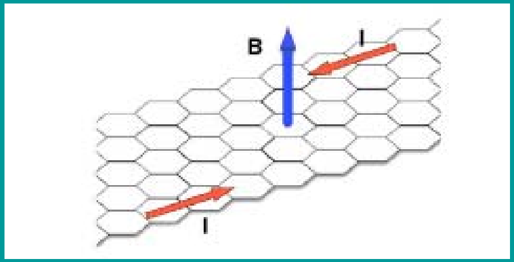

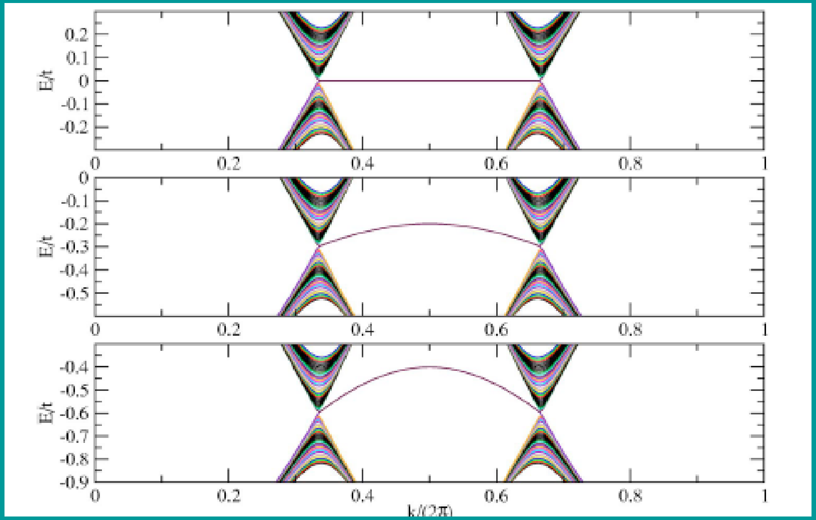

N. M.. R. Peres, F. G., and A. H. Castro Neto, Phys. Rev. B **73**, 125411 (2006)

Boundary conditions at edges

A. R. Akhmerov and C. W. J. Beenakker, Phys. Rev. B **77**, 085423 (2008)

See also:
M. V. Berry and R. J. Mondragon, Proc. R. Soc. London Ser. A **412**, 53 (1987),
E. McCann and V. I. Fal'ko, J. Phys.: Condens. Matter **16**, 2371, (2004),
L. Brey and H. A. Fertig Phys. Rev. B **73**, 235411 (2006)

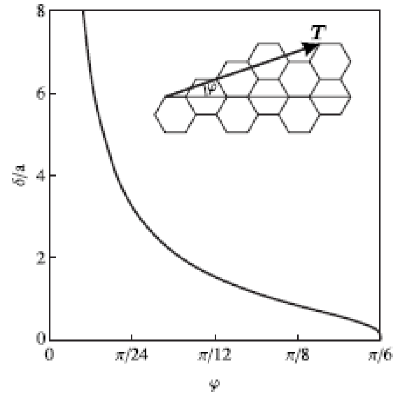

FIG. 2. Dependence on the orientation φ of the distance δ from the boundary within which the zigzag-type boundary condition breaks down. The curve is calculated from formula (3.14) valid in the limit $|\boldsymbol{T}| \gg a$ of large periods. The boundary condition becomes precise upon approaching the zigzag orientation $\varphi = \pi/6$.

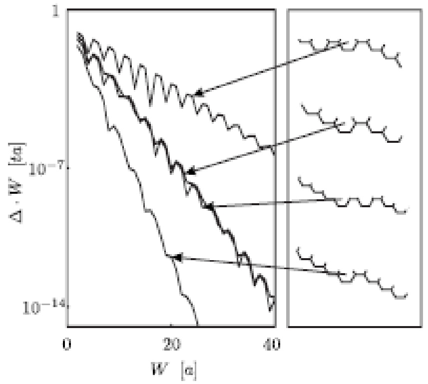

FIG. 7. Dependence of the band gap Δ of zigzaglike nanoribbons on the width W. The curves in the left panel are calculated numerically from the tight-binding equations. The right panel shows the structure of the boundary, repeated periodically along both edges.

From A. R. Akhmerov and C. W. J. Beenakker, Phys. Rev. B **77**, 085423 (2008)

Experiments

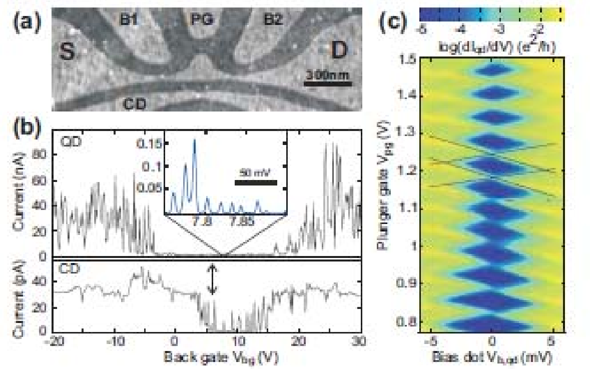

FIG. 1: (Color online) Nanostructured graphene quantum dot device with nanoribbon and characteristic transport measurements. (a) Scanning force micrograph of the measured device. The central island is connected to source (S) and drain (D) contacts by two constrictions. The diameter of the dot is 200 nm and the constrictions are 35 nm wide. The graphene nanoribbon acts as charge detector (CD). Three lateral gates B1, B2 and PG are used to tune the devices. (b) Back gate characteristics of the quantum dot (QD) device (upper panel) and the charge detector (lower panel), shown in (a). Both measurements were performed at a source-drain (bias) voltage of $V_{b,qd} = V_{b,cd} = 500\ \mu$V and at 1.7 K. Inset shows Coulomb blockade resonances observed inside the transport gap as a function of the back gate voltage over a range of 150 mV. (c) Coulomb blockade diamonds in differential conductance (logarithmic scale) recorded as function of the plunger gate and bias voltage with fixed back gate voltage $V_{bg} = 2$ V. The charging energy is estimated to be $E_c \approx 4.3$ meV.

J. Güttinger, C. Stampfer, S. Hellmüller, F. Molitor, T. Ihn and K. Ensslin, Appl. Phys. Lett. **93**, 212102 (2008),
see also:
C. Stampfer, J. Güttinger, F. Molitor, D. Graf, T. Ihn, and K. Ensslin, Appl. Phys. Lett., **92**, 012102 (2008).
C. Stampfer, E. Schurtenberger, F. Molitor, J. Gttinger, T. Ihn, and K. Ensslin, Nano Lett. **8**, 2378 (2008).

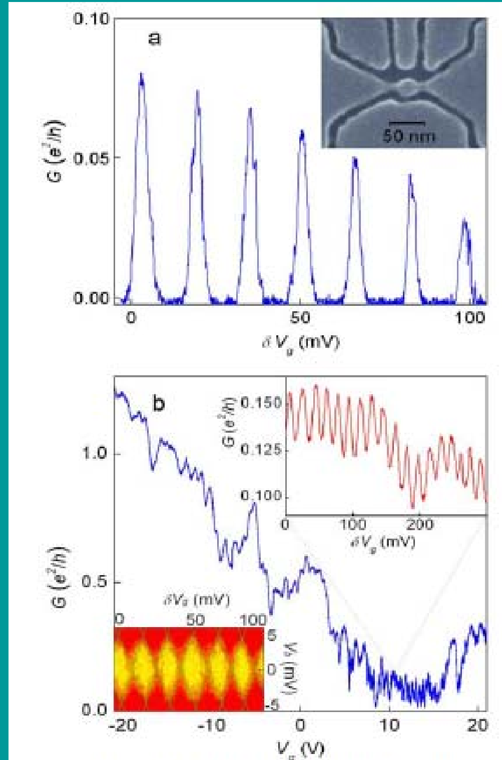

Figure 1. Graphene-based single-electron transistor. a, Conductance G of a device with the central island of 250nm in diameter and distant side gates [SI] as function of V_g in the vicinity of +15V; T =0.3K. The inset shows one of our smaller devices to illustrate the high resolution of our electron-beam lithography that allows features down to 10 nm. Dark areas in the scanning electron micrograph are gaps in the PMMA mask so that graphene is removed from these areas by plasma etching. In this case, a 30-nm QD is connected to contact regions through narrow constrictions and there are 4 side gates. b, Conductance of the same device as in Fig. 1a over a wide range of V_g (T =4K). Upper inset: Zooming into the low-G region reveals hundreds of CB oscillations. The lower inset shows Coulomb diamonds: differential conductance G_{diff} =dI/dV as a function of V_g (around +10V) and bias V_b (yellow-to-red scale corresponds to G_{diff} varying from zero to 0.3e^2/h; note that our color diagrams often appear smudged if printed in gray).

L. A. Ponomarenko, F. Schedin, M. I. Katsnelson, R. Yang, E. H. Hill, K. S. Novoselov, A. K.Geim, Science **320**, 356 (2008)

Ballistic quantum dots

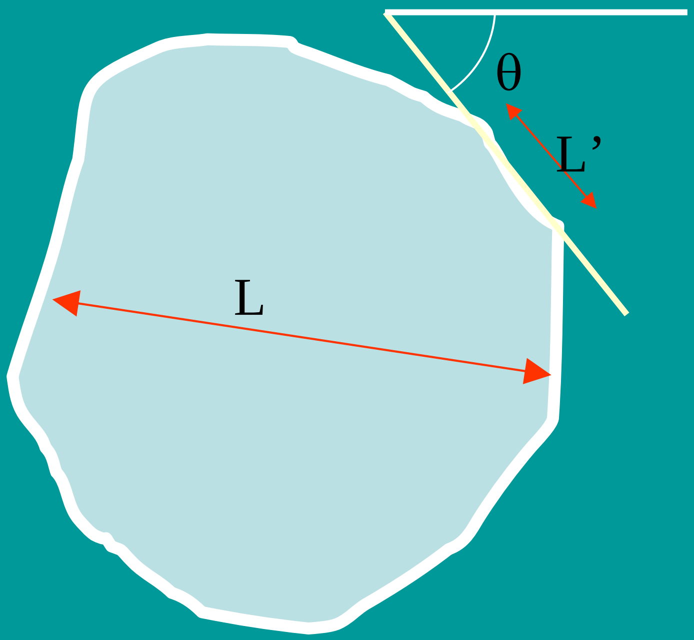

$$\Psi_i\left(r_\parallel, r_\perp\right) \propto e^{ik_i r_\parallel} e^{-\lambda_i r_\perp}$$

$$\varepsilon_i \approx \frac{v_F}{L} e^{-\lambda_i L'}$$

$$\lambda_i \approx c(\theta)\frac{2\pi}{L'} \;,\; c(\theta)\frac{4\pi}{L'}, \ldots, \frac{1}{l(\theta)}$$

$$D(\varepsilon) = \sum_i \delta(\varepsilon - \varepsilon_i) \approx \begin{cases} \dfrac{1}{\varepsilon} & \dfrac{v_F}{L} e^{-L/\bar{l}} \le \varepsilon \le \dfrac{v_F}{L} \\ \dfrac{\varepsilon\, L^2}{v_F^2} & \dfrac{v_F}{L} \le \varepsilon \end{cases}$$

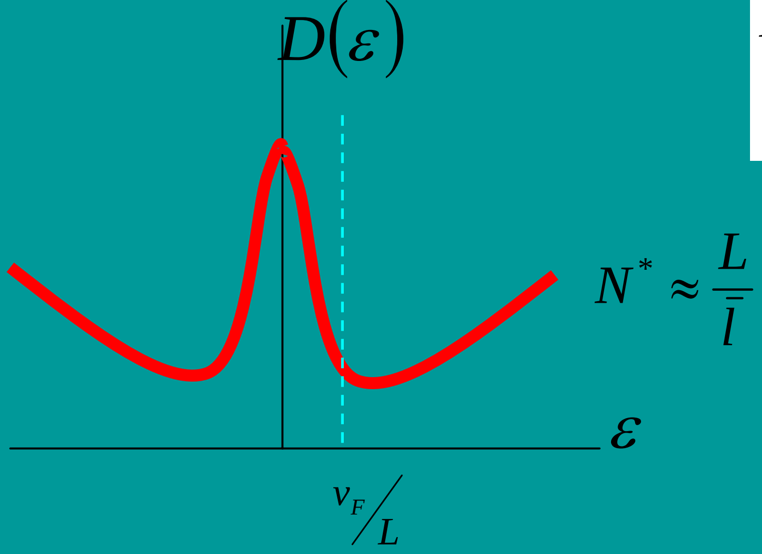

Edges in graphene

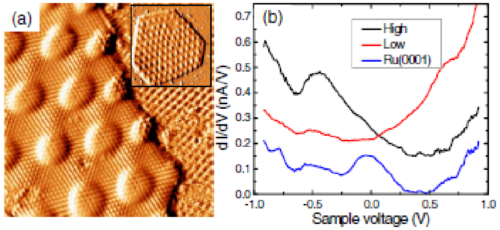

FIG. 4 (color online). (a) 10 nm × 10 nm atomically resolved STM image of a graphene island on Ru(0001). The image was recorded at $V_s = -4.5$ meV and $I_t = 3$ nA. The inset shows an image of the whole island with a lateral size of 47 nm. The images are differentiated in X direction. (b) Spatially resolved tunneling spectra measured on the high (black curve) and low (red curve) areas of the ripples close to the edge of the island and on clean Ruthenium (blue curve). The Ruthenium spectra was offset for clarity.

A. L. Vázquez de Parga, F. Calleja, B. Borca, M. C. G. Passeggi, Jr., J. J. Hinarejos, F. G., and R. Miranda, Phys. Rev. Lett. **100**, 056807 (2008)

Fig. 1. Crystallization and edge formation in graphitic nanoribbons. (**A**) *I* versus *V* curve during Joule heating, indicating three regimes: (i) a linear regime from 1 to 1.25 V, (ii) a slowly increasing slope regime from 1.25 to 1.6 V, and (iii) a rapidly increasing slope regime at 1.6 V. (**B**) Resistance versus input energy at 1.6 V applied bias. (**C**) Ribbon sample before Joule heating, showing very few zigzag (pink lines) and armchair edges (green lines). (**D**) The same ribbon sample after Joule heating (for 10 min at 1.6 V), in which most of the edges seen are either zigzag or armchair edges, as indicated in (**E**). The inset hexagons indicate the zigzag- or armchair-edge orientations associated with the lattice patterns in (C) and (E). (**F**) High-magnification image of the annealed sample showing that well-defined zigzag-armchair and zigzag-zigzag edges are formed. The green hexagons in (E) help with the identification of the atomic structure at the armchair and zigzag edges. Scale bars in (C), (D) and (E), 4 nm; in (F), 1 nm.

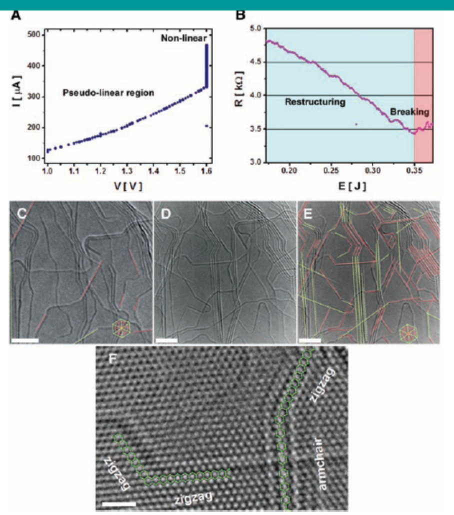

X. Jia, M. Hofmann, V. Meunier, B. G. Sumpter, J. Campos-Delgado, J. M. Romo-Herrera, H. Son, Y.-P. Hsieh, A. Reina, J. Kong, M. Terrones, M. S. Dresselhaus, Science **323**, 1701 (2009)

Fig. 1. (**A**) Aberration-corrected TEM image of a hole in a single layer of graphene produced by prolonged irradiation (frame 1 of Movie S1). Individual carbon atoms are resolved as white spots. Structures lining the perimeter are adsorbates. Scale bar is 5 Å. (Inset) Averaged series of images showing the atomically resolved graphene lattice. (**B**) and (**C**) Two still frames (9 and 10) in the evolution of the hole, with (C) following 4 s after (B). Two carbon atoms (red diamonds in the dashed circle) are removed while two carbon atoms nearby (blue dots) bind to their neighbors to close a hexagon (solid circle). The measured lattice constant is 2.5 Å ± 0.2 Å.

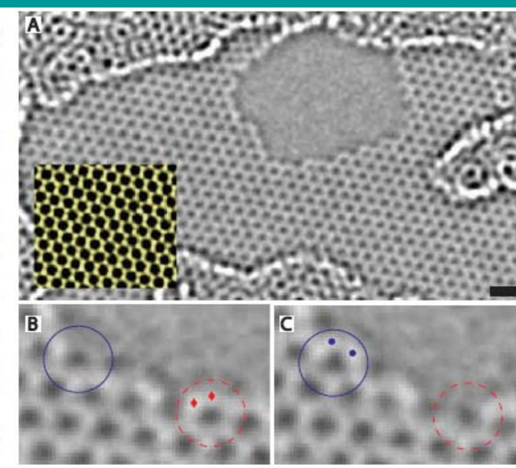

Ç. Ö. Girit, J. C. Meyer, R.Erni, M. D. Rossell, C. Kisielowski, L. Yang, C.-H. Park, M. F. Crommie, M. L. Cohen, S. G. Louie, A. Zettl, Science 323, 1705 (2009)

Ballistic quantum dots. Edge potentials

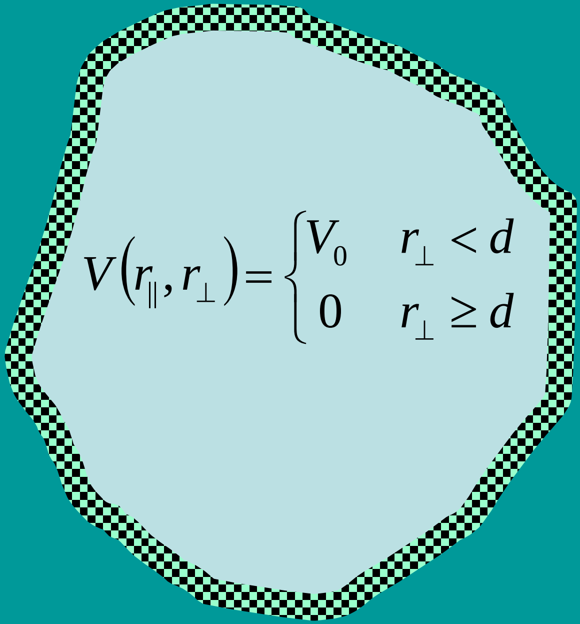

$$V\left(r_{\parallel}, r_{\perp}\right) = \begin{cases} V_0 & r_{\perp} < d \\ 0 & r_{\perp} \ge d \end{cases}$$

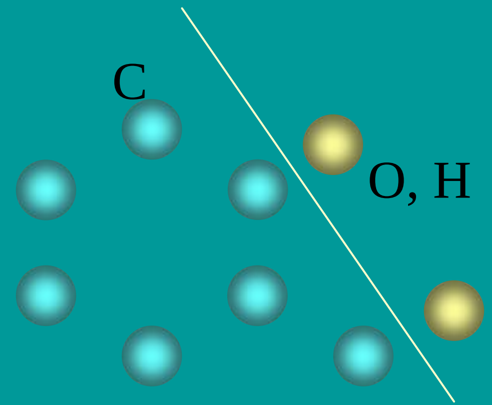

$$\varepsilon_i = \frac{v_F}{L} e^{-\lambda_i L} + V_0 \lambda_i d + t' a^2 \lambda_i^2$$

$$W^* = Max\left(V_0, t'\right)$$

$$l^* = Max(\bar{l}, d)$$

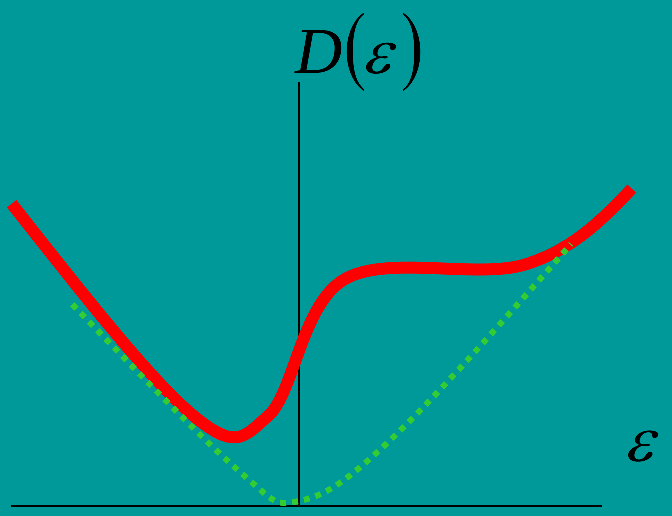

$$D(\varepsilon) \approx \begin{cases} \dfrac{L}{l^*} \dfrac{1}{W^*} + \dfrac{\varepsilon L^2}{v_F^2} & 0 \le \varepsilon \le W^* \\ \dfrac{\varepsilon L^2}{v_F^2} & W^* \le \varepsilon \end{cases}$$

Ballistic quantum dots. Localized states

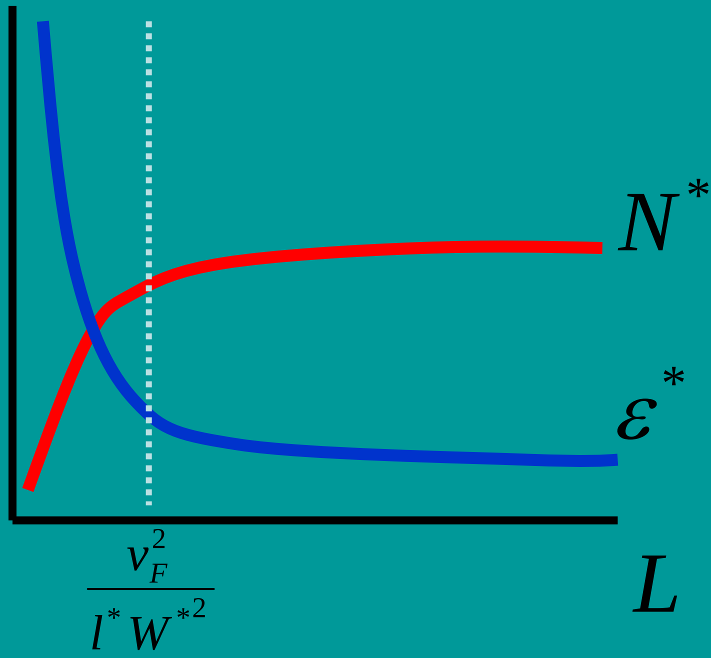

$$\varepsilon^* \approx Min\left(W^*, \frac{v_F^2}{L\, l^* W^*} \right)$$

$$N^* \approx Min\left(\frac{L}{l^*}, \frac{v_F^2}{l^{*2} W^{*2}} \right)$$

$$N^*_{ribbon} \approx Min\left(\frac{L}{l^*}, \frac{v_F^2}{l^{*2} W^{*2}} \frac{L}{W_{ribbon}} \right)$$

There are approximately N^* states localized at the edges, within a range ε^* of the Dirac point

$$L \approx 1\,\mu m$$

$$l^* \approx 0.2\,nm$$

$$W^* \approx 0.3\,eV$$

$$N^* \approx 100$$

$$\varepsilon^* \approx 6\,meV$$

Effective gauge fields

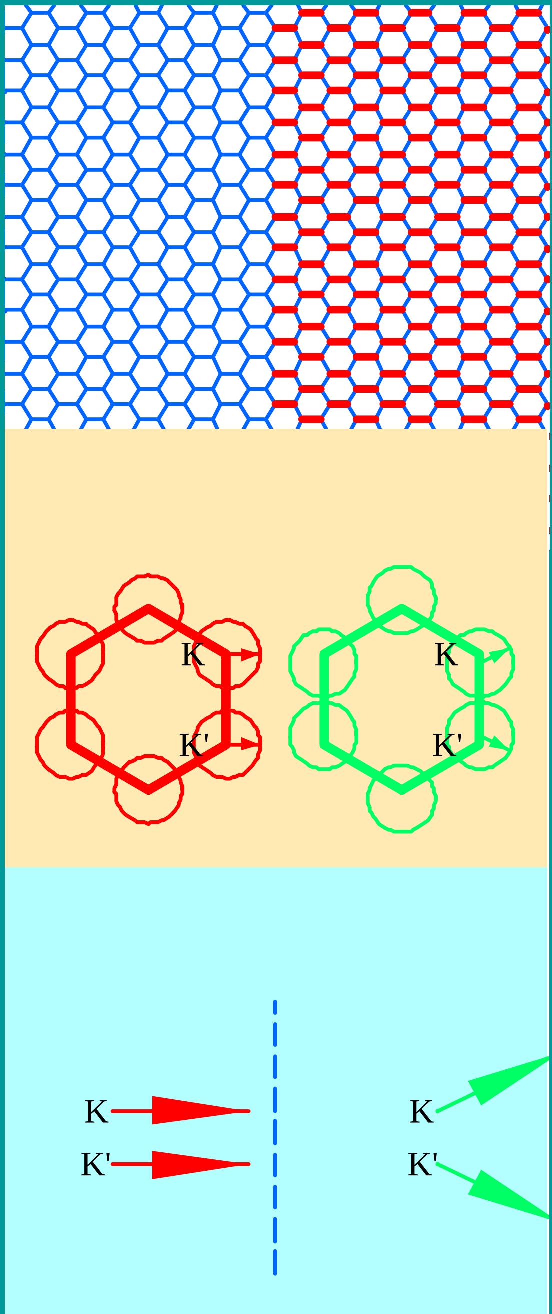

$$H \equiv \begin{pmatrix} 0 & t_1 e^{i\vec{k}_1\vec{a}_1} + t_2 e^{i\vec{k}_2\vec{a}_2} + t_3 e^{i\vec{k}_3\vec{a}_3} \\ t_1 e^{-i\vec{k}_1\vec{a}_1} + t_2 e^{-i\vec{k}_2\vec{a}_2} + t_3 e^{-i\vec{k}_3\vec{a}_3} & 0 \end{pmatrix} \approx$$

$$\begin{pmatrix} 0 & \frac{3\bar{t}a}{2}\left(k_x + ik_y\right) + \Delta t \\ \frac{3\bar{t}a}{2}\left(k_x + ik_y\right) + \Delta t & 0 \end{pmatrix}$$

A modulation of the hoppings leads to a term which modifies the momentum: an effective gauge field.

The induced “magnetic” fields have opposite sign at the two corners of the Brillouin Zone.

These terms are forbidden by symmetry in clean graphene.

Effective electric fields

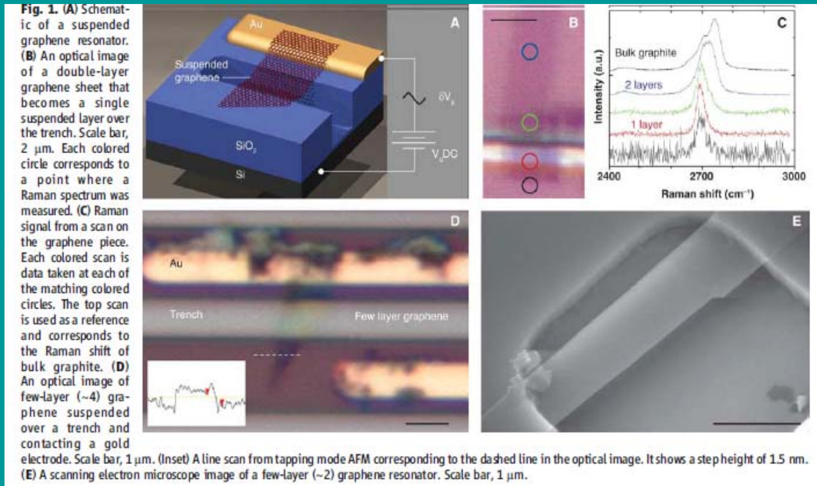

Fig. 1. (**A**) Schematic of a suspended graphene resonator. (**B**) An optical image of a double-layer graphene sheet that becomes a single suspended layer over the trench. Scale bar, 2 μm. Each colored circle corresponds to a point where a Raman spectrum was measured. (**C**) Raman signal from a scan on the graphene piece. Each colored scan is data taken at each of the matching colored circles. The top scan is used as a reference and corresponds to the Raman shift of bulk graphite. (**D**) An optical image of few-layer (~4) graphene suspended over a trench and contacting a gold electrode. Scale bar, 1 μm. (Inset) A line scan from tapping mode AFM corresponding to the dashed line in the optical image. It shows a step height of 1.5 nm. (**E**) A scanning electron microscope image of a few-layer (~2) graphene resonator. Scale bar, 1 μm.

J. Scott Bunch, A. M. van der Zande, Scott S. Verbridge, I. W. Frank, D. M. Tanenbaum, J. M. Parpia, H. G. Craighead, P. L. McEuen, Science **315**, 490 (2007)

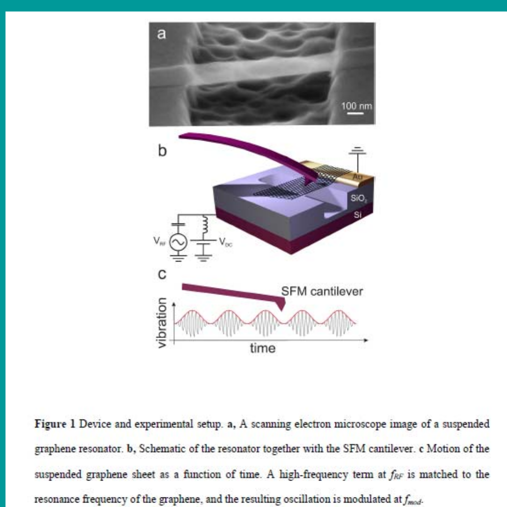

Figure 1 Device and experimental setup. **a**, A scanning electron microscope image of a suspended graphene resonator. **b**, Schematic of the resonator together with the SFM cantilever. **c** Motion of the suspended graphene sheet as a function of time. A high-frequency term at f_{RF} is matched to the resonance frequency of the graphene, and the resulting oscillation is modulated at f_{mod}.

D. García-Sánchez, A. M. van der Zande, A. San Paulo, B. Lassagne, P. L. McEuen, A. Bachtold, Nano Lett. **8**, 1399 (2008)

$$H_K \equiv \begin{pmatrix} V\sum_i u_{ii} & v_F\left(-i\partial_x - \partial_y - A_x + iA_y\right) \\ v_F\left(-i\partial_x + \partial_y - A_x - iA_y\right) & V\sum_i u_{ii} \end{pmatrix}$$

$$A_x = \frac{\beta}{2a}\left(u_{xx} - u_{yy}\right) \qquad A_y = \frac{\beta}{2a} 2u_{xy}$$

$$V \approx 10-20\,eV \qquad \beta = \frac{\partial \log(t)}{\partial \log(a)} \approx 2-3$$

H. Suzuura and T. Ando, Phys. Rev. B **65**, 235412 (2002)
J. L. Mañes, Phys. Rev. B **76**, 045430 (2007)

$$\vec{E} = -V\nabla\left(\sum_i u_{ii}\right) \pm \frac{\partial \vec{A}}{\partial t}$$

$$\left|\vec{E}_{\vec{q}}\right| \approx \left(V\left|\vec{q}\right|^2 \times \frac{\left|\vec{q}\right|}{k_{FT}} \pm \frac{N\beta}{2a}\left|\vec{q}\right|\omega_{\vec{q}}\right)\left|\vec{B}\right|_{\vec{q}}$$

$$\omega_{\vec{q}} = c\left|\vec{q}\right| \approx \frac{c}{L}$$

screening

$$\frac{E_{gauge}}{E_{scalar}} \approx N\beta \frac{c\,a^{-1}}{V/k_{FT}L} \approx N\beta \frac{\theta_{Debye}}{V} k_{FT}L >> 1$$

Energy dissipation

$$D = v_F^2 \frac{\tau \tau_V}{\tau + \tau_V}$$

$$\sigma_{DC} = \nu D$$

$$\frac{1}{\tau_V} \approx \frac{1}{\tau_{V0}} + c \frac{T^2}{E_F}$$

$$\frac{dW}{dt} = \vec{j}\vec{E} = \omega_{\vec{q}} \Gamma_{\vec{q}}$$

Valley drag: K. Flensberg, B. Y.-K. Hu, A.-P. Jauho, J. M. Kinaret, Phys. Rev. B **52**, 14761 (1995)
A. Kamenev, Y. Oreg, Phys. Rev. B **52**, 7516 (1995)
W.-K. Tse, Y.-K. Yu, and S. Das Sarma, Phys. Rev. B.**76**, 081401 (2008)

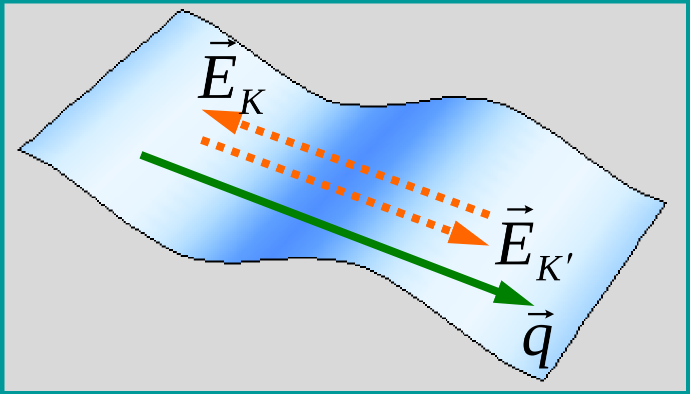

Longitudinal polarization

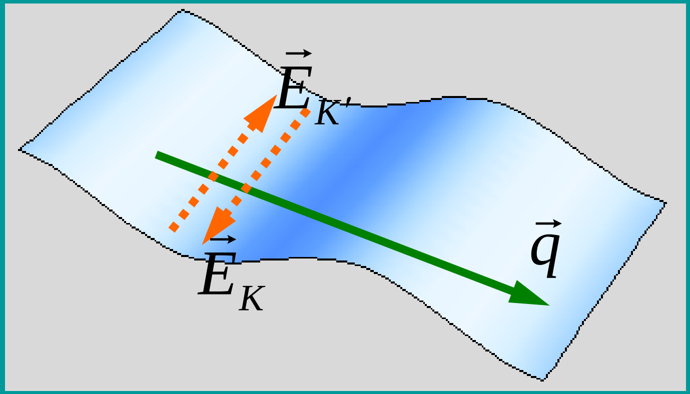

Transverse polarization

Conductivity

See: B. I. Halperin, Patrick A. Lee, and N. Read, Phys. Rev. **47**, 7312 (1993)

$$\frac{\partial n_K}{\partial t} + \nabla \vec{j}_K = -\frac{1}{\tau_V}\left(n_K - n_{K'}\right)$$

$$\frac{\partial n_{K'}}{\partial t} + \nabla \vec{j}_{K'} = -\frac{1}{\tau_V}\left(n_{K'} - n_K\right)$$

Continuity

Ohm's law

$$\left(\frac{1}{\tau} + \frac{1}{\tau_V}\right)\vec{j}_K - \frac{1}{\tau_V}\vec{j}_{K'} = -\frac{v_F^2}{2}\nabla n_K + \frac{e^2 \nu v_F^2}{2}\vec{E}_K$$

$$-\frac{1}{\tau_V}\vec{j}_K + \left(\frac{1}{\tau} + \frac{1}{\tau_V}\right)\vec{j}_{K'} = -\frac{v_F^2}{2}\nabla n_{K'} + \frac{e^2 \nu v_F^2}{2}\vec{E}_{K'}$$

$$\sigma_{\parallel}(\vec{q},\omega) = \sigma_{DC}\frac{\left[\omega^2 + \frac{2}{\tau_V}\left(D|\vec{q}|^2 + \frac{2}{\tau_V}\right)\right]}{\omega^2 + \left(D|\vec{q}|^2 + \frac{2}{\tau_V}\right)^2}$$

Longitudinal polarization

$$\sigma_{\perp}(\vec{q},\omega) = \sigma_{DC}$$

Transverse polarization

Ballistic limit:

$$D|\vec{q}|^2 \leftrightarrow v_F|\vec{q}|$$

$$l \leftrightarrow |\vec{q}|^{-1}$$

Quality factor

$$n = 10^{12}\,cm^{-2}$$

$$\tau_V^{-1} = \frac{1}{10\tau} + \frac{T^2}{E_F}$$

$$L = q^{-1} = 1\mu m$$

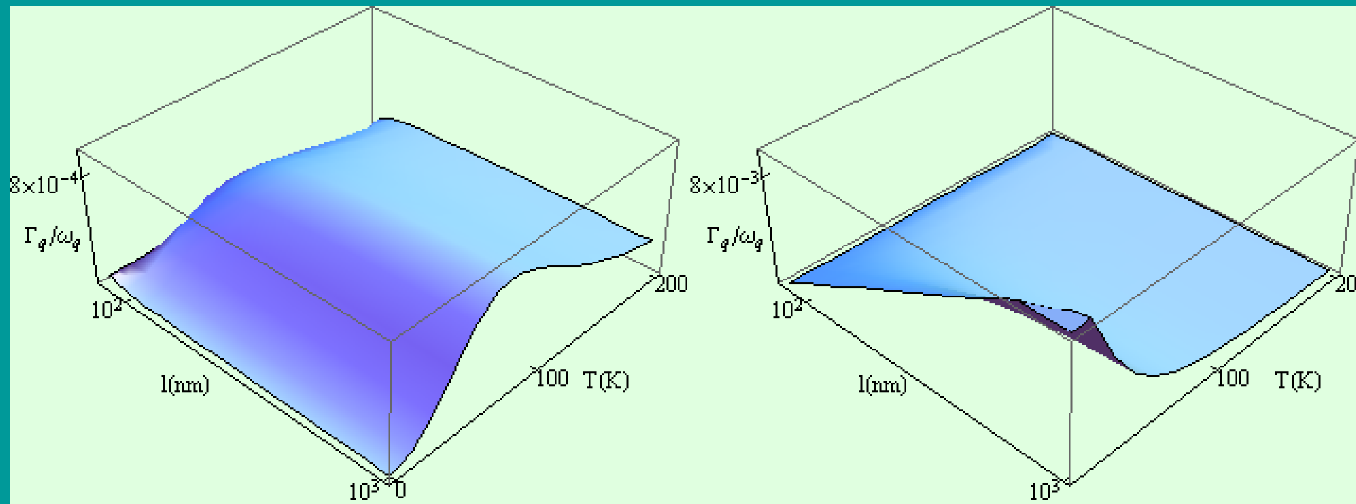

Longitudinal polarization   Transverse polarization

Semiclassical analysis
Valid for multilayered systems

Suspended graphene. Graphene membranes

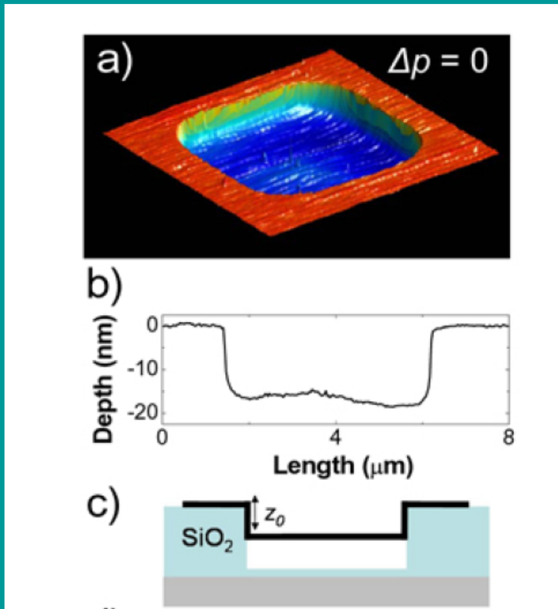

J. S. Bunch, S. S. Verbridge, J. S. Alden, A. M. van der Zande, J. M. Parpia, H. G. Craighead, and P. L. McEuen, Nano Lett. **8**, 2458 (2008)

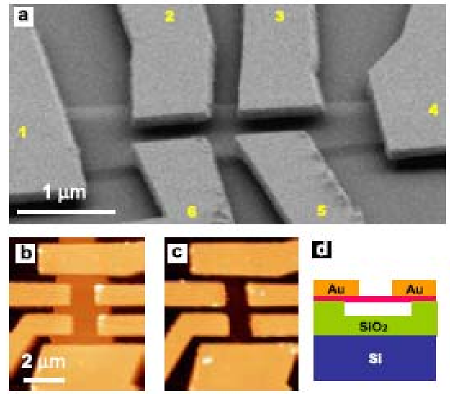

FIG. 1: (a) SEM image of a typical suspended six-probe graphene device taken at 15° with respect to the sample plane. (b) AFM image of the suspended device #1 before the measurements. (c) AFM image of the device #1 after the measurements with graphene removed by a short oxygen plasma etch (same z scale). (d) Device schematic, side-view. Degenerately doped silicon gate (blue), partly etched SiO_2 (green), suspended single-layer graphene (pink) and Au/Cr electrodes (orange).

K. I. Bolotin, K. J. Sikes, Z. Jiang, G. Fudenberg, J. Hone, P. Kim, and H. L. Stormer, Solid St. Commun. **146**, 351 (2008)

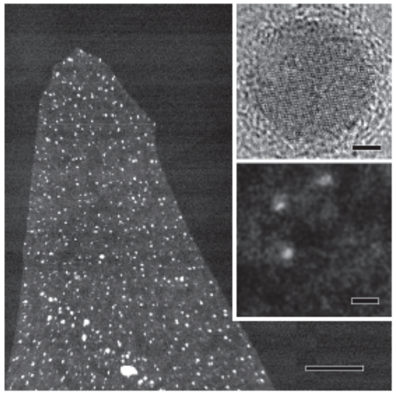

Figure 4: HAADF micrograph of a section of a graphene membrane that fractured during annealing. The graphene crystal is supported from one side only. White dots are copper nanoparticles. Scale bar: 1μm. Top inset: high resolution bright field STEM micrograph of such a Cu particle (⌀ 8.0 nm; scale bar: 2 nm). Low inset: HAADF image of individual atoms on graphene; scale bar: 2 Å.

T. J. Booth, P. Blake, R. R. Nair, D. Jiang, E. W. Hill, U. Bangert, A. Bleloch, M. Gass, K. S. Novoselov, M. I. Katsnelson, and A. K. Geim, Nano Lett. **8**, 2442 (2008)

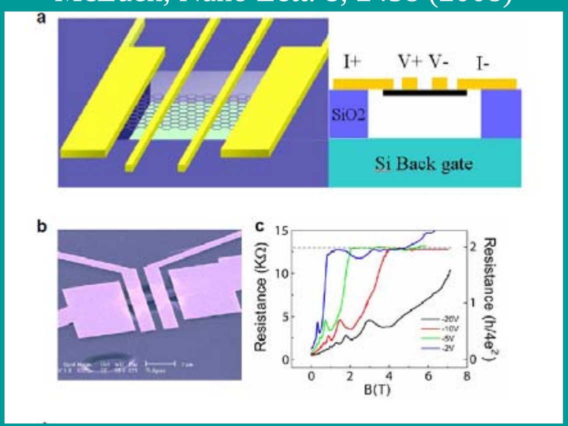

X. Du, I. Skachko, A. Barker, E. Y. Andrei, Nature Nanotechnology **3**, 491 (2008)

Suspended graphene. Graphene membranes

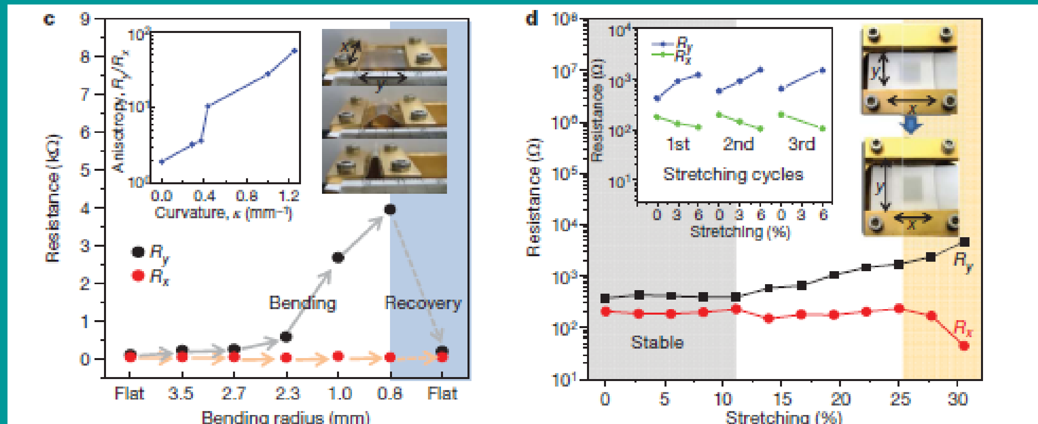

K. S. Kim, Y. Zhao, H. Jang, S. Y. Lee, J. M. Kim, K. S. Kim, J. H. Ahn, P. Kim, J.-Y. Choi, B. H. Hong, Nature **457**, 706 (2008)

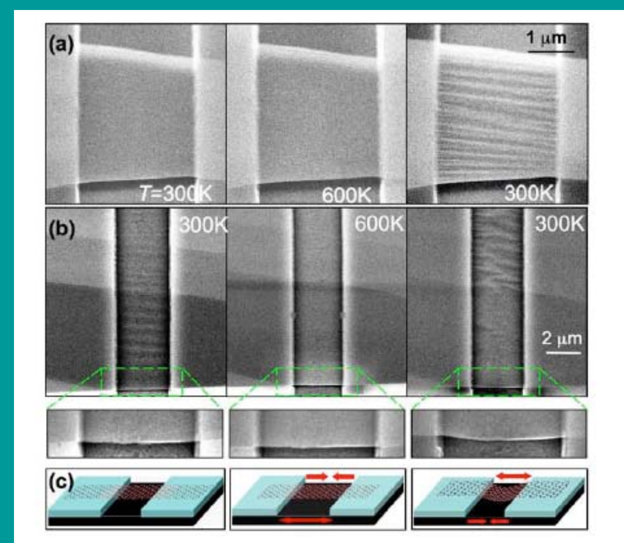

W. Bao, F. Miao, Z. Chen, H. Zhang, W. Jang, C. Dames, C. N. Lau, arXiv:0903.0414

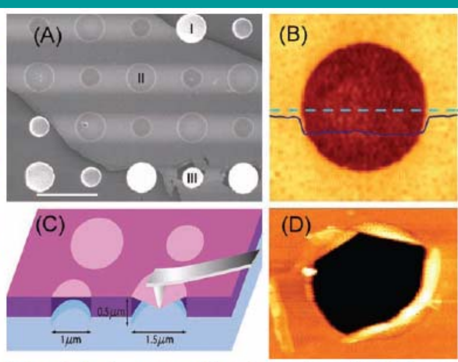

Fig. 1. Images of suspended graphene membranes. **(A)** Scanning electron micrograph of a large graphene flake spanning an array of circular holes 1 μm and 1.5 μm in diameter. Area I shows a hole partially covered by graphene, area II is fully covered, and area III is fractured from indentation. Scale bar, 3 μm. **(B)** Noncontact mode AFM image of one membrane, 1.5 μm in diameter. The solid blue line is a height profile along the dashed line. The step height at the edge of the membrane is about 2.5 nm. **(C)** Schematic of nanoindentation on suspended graphene membrane. **(D)** AFM image of a fractured membrane.

C. Lee, X. Wei, J. W. Kysar, J. Hone, Science **321**, 385 (2008)

Ballistic transport in suspended graphene

M. M. Fogler, F. G., M. I. Katsnelson, Phys. Rev. Lett. **101**, 226804 (2008)

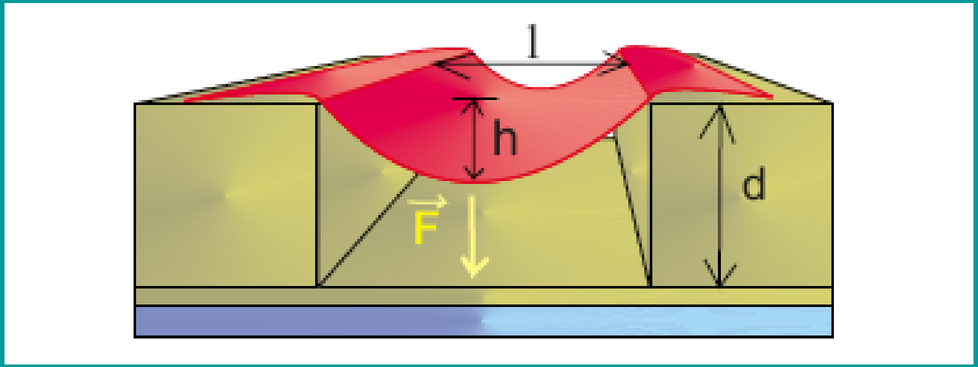

- The graphene layer is deformed by the applied electric field, slack, …
- Stresses lead to effective gauge potentials

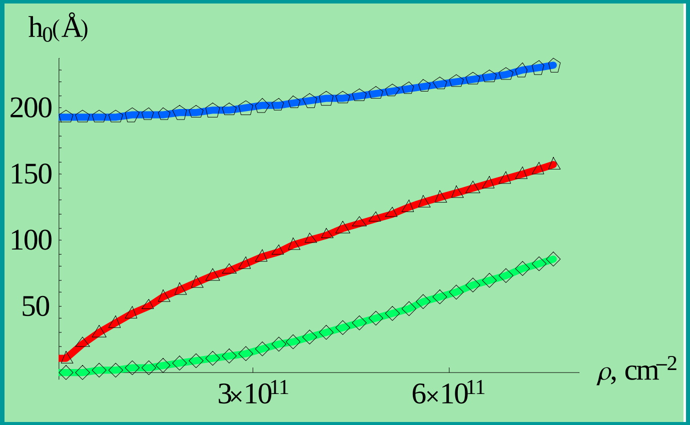

Maximum height as function of carrier density for different values of the slack

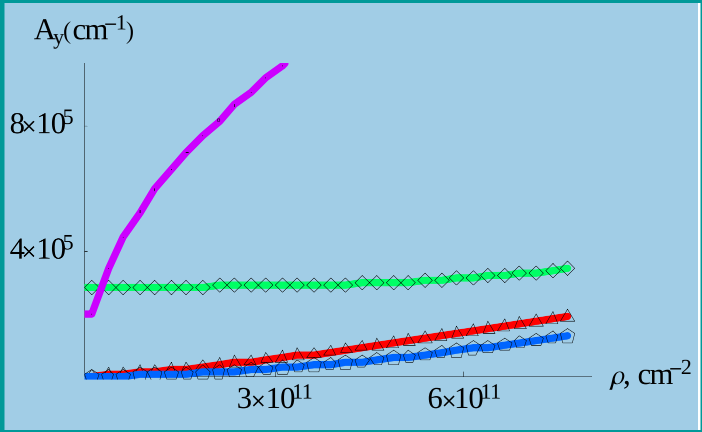

Vector potential inside the suspended region as function of carrier density for different values of the slack

Ballistic transport in suspended graphene

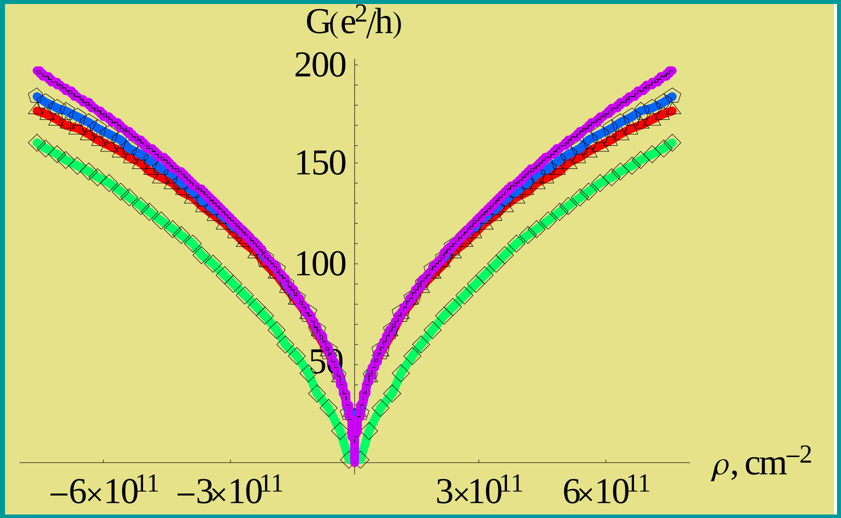

Transmission through a deformed graphene sheet as function of density for different values of the slack

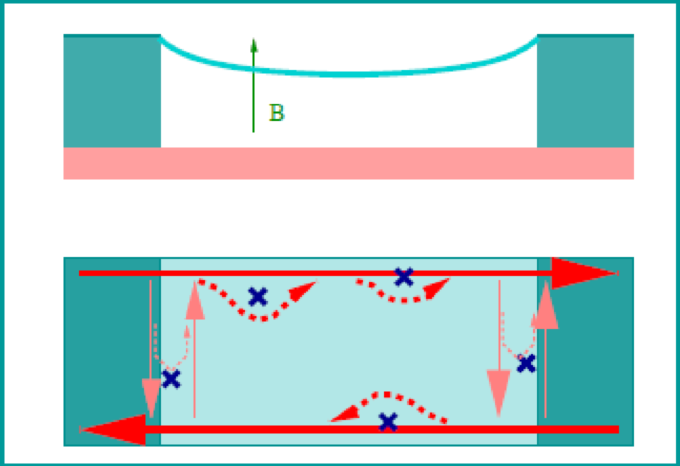

Hall currents in a magnetic field

Effects of a real magnetic field

G. León, E. Prada, P. San José, F. G., unpublished

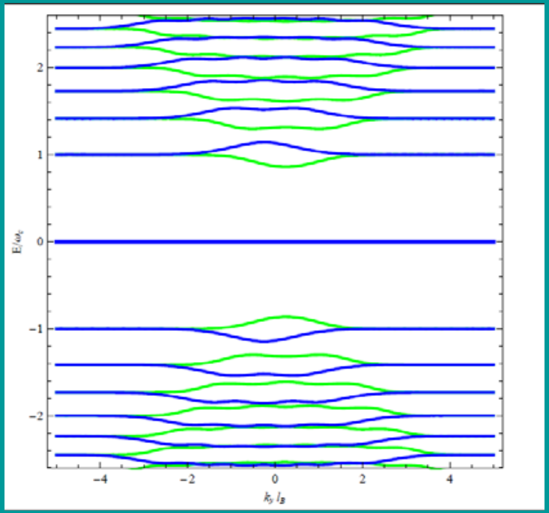

Landau levels as function of the momentum parallel to the boundary

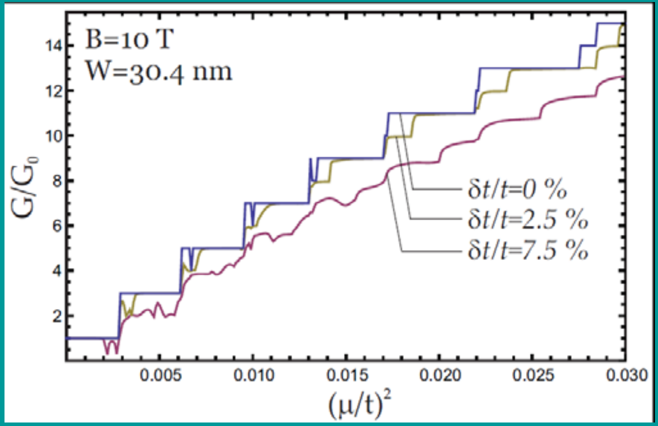

Integer Quantum Hall steps in a graphene ribbon where part of it is under a constant stress

Effective magnetic fields in strained graphene

A. K. Geim, M. I. Katsnelson, F. G., unpublished

$$u_r(r,\theta) = Ar^2 \sin(3\theta)$$
$$u_\theta(r,\theta) = Ar^2 \cos(3\theta)$$
$$\sigma_{rr}(r,\theta) = 4\mu Ar \sin(3\theta)$$
$$\sigma_{\theta\theta}(r,\theta) = -4\mu Ar \sin(3\theta)$$
$$\sigma_{r\theta}(r,\theta) = 4\mu Ar \cos(3\theta)$$

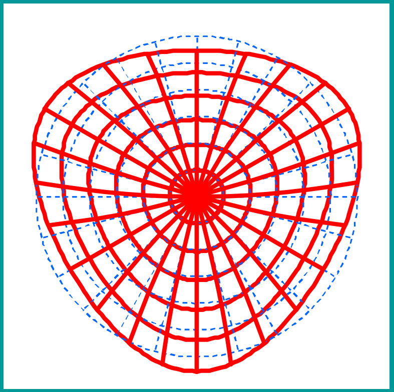

$$u_x(x,y) = 2Axy$$
$$u_y(x,y) = A(x^2 - y^2)$$
$$\sigma_{xx}(x,y) = 4\mu Ay$$
$$\sigma_{yy}(x,y) = -4\mu Ay$$
$$\sigma_{xy}(x,y) = 4\mu Ax$$

Shear deformation: Constant effective magnetic field

$$l_B \approx \sqrt{\frac{aR}{8\bar{u}\beta}}$$
$$R \approx 1\mu m, \quad a \approx 0.1nm, \quad \beta \approx 3, \quad \bar{u} \approx 0.1$$
$$l_B \approx 7nm, \quad B \approx 10T$$

Dependence on boundary conditions:

Applied forces

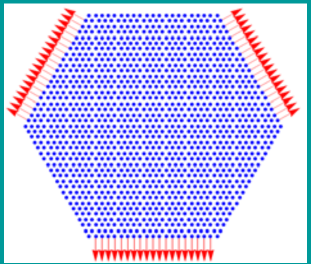

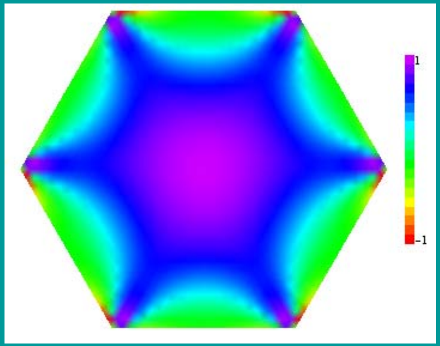

Effective magnetic field

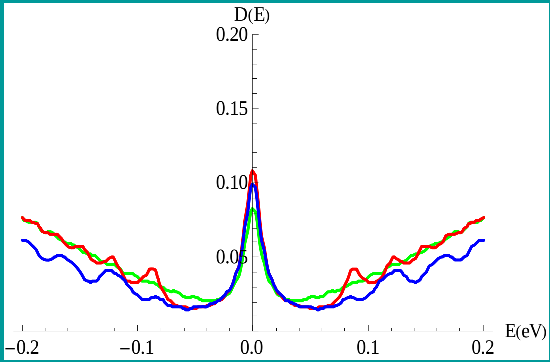

Total density of states

Strain superlattices

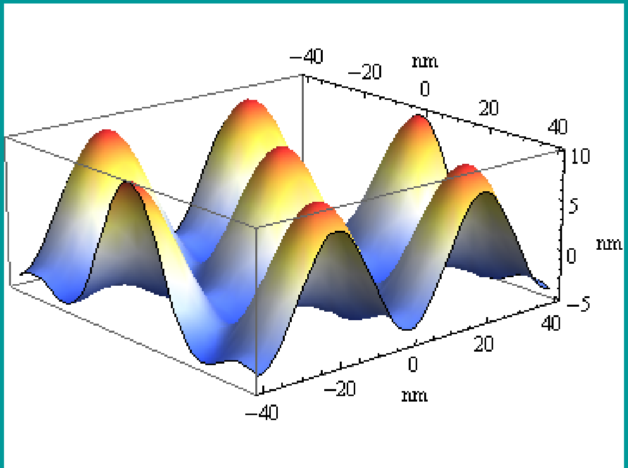

Height modulations

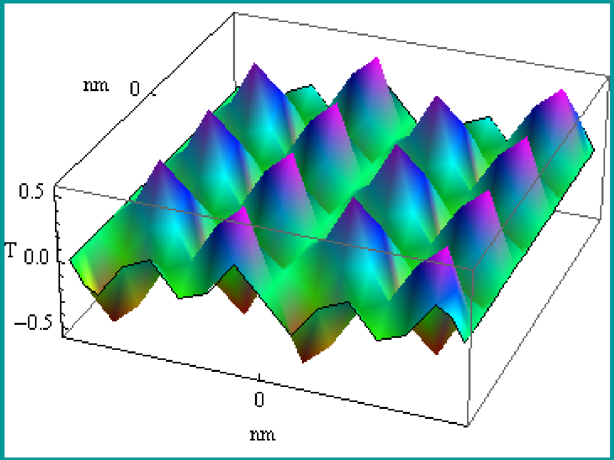

Effective magnetic field

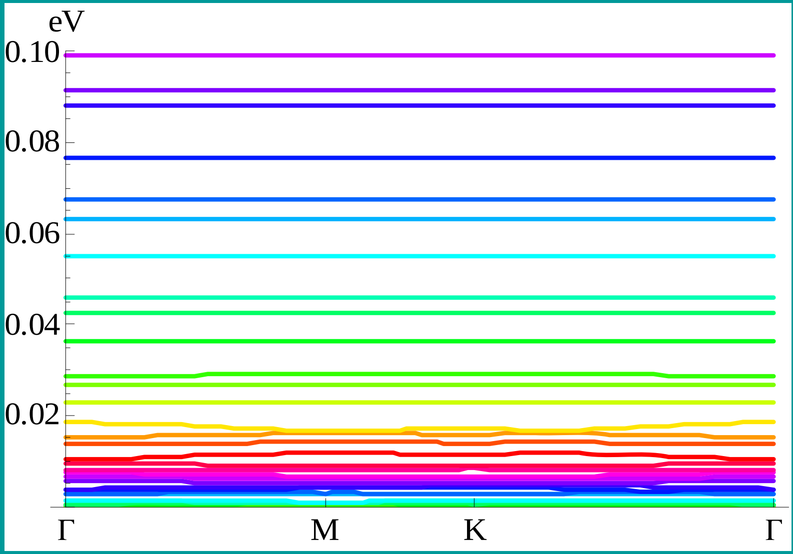

Electronic bands

Wrinkles and mechanical instabilities in strained graphene

F. G., B. Horovitz, P. Le Doussal, arXiv:0811.4670, Solid St. Commun., in press

Wrinkling instability:

E.Cerda and L. Mahadevan, Phys. Rev. Lett. **90**, 074302 (2003)
T. A. Witten, Rev. Mod. Phys. **79**, 643 (2007)

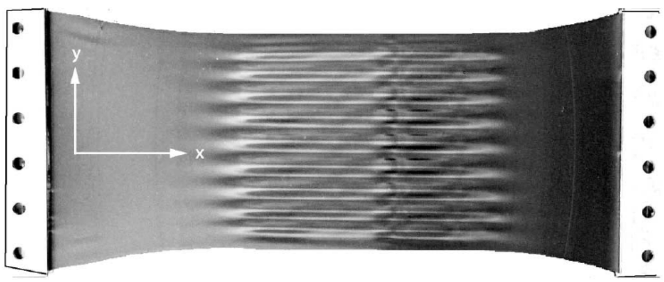

FIG. 1. Wrinkles in a polyethylene sheet of length $L \approx 25$ cm, width $W \approx 10$ cm, and thickness $t \approx 0.01$ cm under a uniaxial tensile strain $\gamma \approx 0.10$. (Figure courtesy of K. Ravi-Chandar)

E.Cerda and L. Mahadevan, Phys. Rev. Lett. **90**, 074302 (2003)

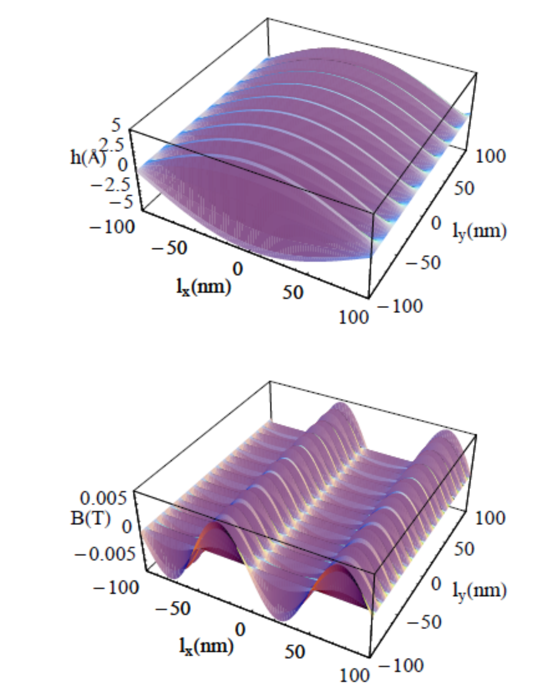

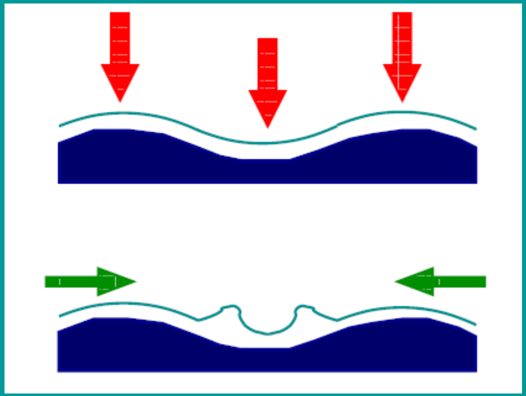

Possible instabilities in graphene on a substrate

- Localized states at edges can lead to observable consequences in graphene quantum dots

- Synthetic electric fields are induced in vibrating graphene. They give a simple physical picture of dissipation mechanisms.

- Synthetic magnetic fields interfere with real magnetic fields in suspended samples, modifying the properties in the Quantum Hall regime.